



# One-step synthesis, characterizations and mechanistic study of nanosheets-constructed fluffy ZnO and Ag/ZnO spheres used for Rhodamine B photodegradation

Youlei Lai, Ming Meng\*, Yifu Yu

Tianjin Key Laboratory of Applied Catalysis Science & Engineering, School of Chemical Engineering & Technology, Tianjin University, Tianjin 300072, PR China

## ARTICLE INFO

### Article history:

Received 5 June 2010

Received in revised form 27 August 2010

Accepted 29 August 2010

Available online 27 September 2010

### Keywords:

Zinc oxide

Silver

Hierarchical structure

Mechanism

Photocatalysis

## ABSTRACT

Nanosheets-constructed ZnO spheres with novel three-dimensional (3D) fluffy structure were successfully synthesized by a facile one-step solvothermal method. Each fluffy ZnO sphere possesses a diameter of 2–3  $\mu\text{m}$ , consisting of crossed nanosheets with an average thickness of  $\sim 20$  nm. Such special hollow 3D structure makes larger surface area and more active sites exposed during the reaction, facilitating the transportation of reactants and products and increasing the reaction rate. The activity measurement for Rhodamine B photodegradation shows that such fluffy ZnO spheres do possess much higher photocatalytic activity than other commonly reported nanostructured ZnO, such as nanoflowers, nanospiraldisks, nanodumbbells and nanorods. The results of photoluminescence spectra show that the fluffy spheres show much higher electron–hole segregation efficiency than other ZnO materials. Through one-pot synthesis Ag is readily doped on the fluffy spheres and strongly interacts with them, further improving the photocatalytic performance of ZnO. Based on the properties and characterization results, a special growth mechanism for such fluffy ZnO spheres is proposed, and the photocatalytic reaction mechanism is also discussed.

© 2010 Elsevier B.V. All rights reserved.

## 1. Introduction

Zinc oxide (ZnO) with a direct wide band gap (3.37 eV) and a large exciton binding energy (60 meV) is a very important II–VI semiconductor [1]. In the last several years, it has been extensively investigated because of its promising applications in new energy development and environmental pollution control. Recently, ZnO has attracted much attention with respect to its photocatalytic activity. As a photocatalyst, it can directly degrade various pollutants effectively in wastewater through simple photocatalytic oxidation and reduction reactions. Compared with traditional methods such as adsorption, filter and sedimentation, photocatalytic degradation can directly eliminate the secondary pollution without further treatment, largely decreasing the process cost [2].

When the light energy is equal to or higher than the band gap of semiconductor, the electrons of the valence band (VB) can be excited to the conduction band (CB). Some of these photogenerated electrons and holes can migrate to the surface of the semiconductor and be trapped by the oxygen and surface hydroxyl, respectively, forming the hydroxide free radical  $\cdot\text{OH}$  which is active species for

the degradation of dye pollutants. However, some of these photo-generated electrons and holes are inclined to recombine inside or on the surface of the semiconductor, thus decreasing the photocatalytic efficiency. Therefore, large specific surface area and high segregation efficiency of photogenerated electrons and holes are necessary for a good photocatalyst [3].

Due to the unique and different properties of nanostructured ZnO from the bulk ZnO, such as small size effect, surface effect, quantum effect and macroscopic quantum tunnel effect, nanostructured ZnO has attracted much attention. Since the mean free path of electrons is also in nanoscale, the photogenerated electrons and holes can easily arrive at the surface of these nanosized ZnO for reaction [4,5], which reduces the possibility of electron–hole recombination and enhances the photocatalytic efficiency. Moreover, nanosized ZnO photocatalysts often possess higher surface-to-volume ratio than the bulk ZnO, supplying more active sites on the surface, and therefore remarkably increasing the degradation rate of pollutants. However, these nanosized materials (such as nanorods, nanoparticles and nanosheets) are inclined to aggregate during growth or photocatalytic reaction process, leading to the reduction of the specific surface area, and counteracting the enhancement effect for photocatalytic performance [3,6]. An effective way to keep high specific surface area or prevent aggregation is to assemble these nanosized units to form three-dimensional (3D) hierarchical micro/nanostructure.

\* Corresponding author. Tel.: +86 022 2789 2275; fax: +86 022 2789 2275.

E-mail address: [mengm@tju.edu.cn](mailto:mengm@tju.edu.cn) (M. Meng).

During the past several years, lots of methods have been developed for the preparation of ZnO with 3D hierarchical micro/nanostructures, and various structures have been fabricated, such as nanotetrapods, core/shell structures, “dandelions” and bionic structures [5–8]. However, these methods are often based on tedious operations and rigorous experimental conditions (such as expensive substrate, difficult template selecting and high temperature, etc.). One-step synthesis of these 3D hierarchical micro/nanostructures in an economical way is still a great challenge. As a facile, low-temperature, economical and potential large-scale industrialization method for nano-materials synthesis, wet chemical method, especially the hydrothermal or solvothermal method, has attracted particular attention in recent years.

It has been reported that citric acid with carboxyl groups as capping agent in aqueous solution can adsorb on the surface of wurtzite ZnO, which causes the formation of platy crystals but not nanorods [9]. However, the influence of citric acid on ZnO crystal growth in alcoholic solution is still unclear. In this work, a novel fluffy ZnO 3D hierarchical micro/nanostructure was successfully fabricated by a facile solvothermal method using ethanol and water as solution while citric acid as capping agent. It is reported that after Ag doped on ZnO the photogenerated electrons in the CB of ZnO can transfer to the Ag islands, the doped Ag can act as the sink to store photogenerated electrons, effectively inhibiting electron–hole recombination and enhancing the segregation efficiency [3,10,11]. Therefore, in the present work the fluffy ZnO modified with Ag was also synthesized by the same one-step method. It is found that the fluffy ZnO spheres show much better photocatalytic activity than other nanostructured ZnO materials; doping with Ag can further increase the photocatalytic performance of such fluffy ZnO. The synthesized materials are characterized by many techniques, such as nitrogen adsorption/desorption, X-ray diffraction (XRD), field-emission scanning electron microscopy (FESEM), transmission electron microscopy (TEM), energy-dispersive X-ray spectroscopy (EDS), X-ray photoelectron spectroscopy (XPS), UV–vis diffuse reflectance spectroscopy (UV–vis DRS), Fourier transform infrared spectroscopy (FT-IR), thermogravimetry (TG) and room temperature photoluminescence spectra (PL). Based on the characterization results, a special growth mechanism of such fluffy ZnO spheres is proposed and the photocatalytic mechanism of such ZnO and Ag/ZnO is also discussed.

## 2. Experimental

### 2.1. Catalyst synthesis

All the reagents used in this work are in analytical grade without further purification (supplied by Tianjin Guangfu Fine Chemical Research Institute). The detailed synthesis procedure is as follows: zinc acetate dihydrate (0.8 g) and citric acid (0.6 g) were dissolved in distilled water (50 mL), and then absolute ethanol (10 mL) and sodium hydroxide aqueous solution (1 mol L<sup>-1</sup>, 20 mL) were dropped into the solution under vigorous stirring. The obtained suspension was transferred to a 100 mL Teflon-sealed autoclave and maintained at 120 °C for 24 h. The resulting products were centrifuged, washed with water and ethanol in turns and dried at room temperature for further characterization. This sample is denoted as ZnO-f. A series of Ag/ZnO samples were prepared by one-pot synthesis method for understanding the influence of Ag on the photocatalytic activity. The preparation procedure is the same as that for ZnO-f. The sole difference is the addition of certain amounts of silver nitrate into the mixed solution of zinc acetate dihydrate and citric acid at the first step. This series of samples are denoted as

ZA1, ZA3, ZA5, ZA7, ZA9 according to the Ag/Zn atomic ratio of 1%, 3%, 5%, 7% or 9%, respectively.

For comparison, the ZnO samples with different morphologies were also prepared:

The ZnO nanorods were synthesized at the same synthesis condition as that for ZnO-f but without using citric acid as capping agent.

The ZnO nanoflowers were also synthesized at the same synthesis condition as that for ZnO-f but without using ethanol solution and citric acid as solvent and capping agent.

The ZnO nanospiraldisks were synthesized as follows: zinc acetate dihydrate (0.8 g) was dissolved in distilled water, ammonia aqueous solution (28 wt.%, 2.5 mL) was added dropwise to the above solution. The obtained suspension (80 mL) was transferred to a 100 mL Teflon-sealed autoclave and maintained at 120 °C for 10 h. The resulting products were centrifuged, washed with water and ethanol in turns and dried at room temperature.

The ZnO nanodumbbells were also synthesized by this facile method for comparison: potassium citrate (2.3 g) was dissolved in distilled water and adjusting the pH value of the solution to 7.5 by ammonia aqueous solution (28 wt.%, 2.5 mL). The obtained suspension (80 mL) was transferred to a 100 mL Teflon-sealed autoclave and maintained at 120 °C for 18 h.

### 2.2. Catalyst characterization

The X-ray powder diffraction (XRD) was performed on an X'pert Pro rotatory diffractometer (PANalytical Company) operating at 50 mA and 30 kV using Co K $\alpha$  as radiation source ( $\lambda = 0.17890$  nm). The data of  $2\theta$  from 20 to 100° were collected with the stepsize of 0.033°.

The surface morphology was determined with a Nanosem 430 field-emission scanning electron microscope (SEM). TEM and HR-TEM images were obtained using a Philips Tecnai G<sup>2</sup>F20 system equipped with energy-dispersive X-ray spectroscopy (EDX) operating at 200 kV. Before observation, the sample was ultrasonically suspended and deposited on a carbon film supported on a copper grid.

Specific surface area and pore size distribution were measured by nitrogen adsorption/desorption at 77 K using a Quantachrome NOVA-2000 instrument. The samples were degassed at 100 °C for 12 h prior to the adsorption experiments. The specific surface area ( $S_{\text{BET}}$ ) was calculated by BET method in 0–0.3 partial pressure range, and the pore size distribution was determined by Barrett–Joyner–Halenda (BJH) method from the desorption branch of the isotherm.

X-ray photoelectron spectra (XPS) were recorded on a PHI-1600 ESCA spectrometer using Mg K $\alpha$  radiation (1253.6 eV). The binding energies were calibrated using C1s peak of contaminant carbon (B.E. = 284.6 eV) as standard.

UV–vis diffuse reflectance spectra (DRS) were recorded by means of a Lambda 750S (Perkin-Elmer) UV–vis spectrometer equipped with an integrating sphere. The DRS spectra were collected in the range of 200–800 nm against barium sulfate standard.

Fourier transform infrared spectra (FT-IR) were obtained on a Nicolet Nexus spectrometer using KBr as reference. A certain amount of powder sample (1 mg) and KBr (100 mg) was ground together and then compressed into tablet before measurement.

Thermogravimetric analysis (TG) was conducted using a Pyris Diamond TG/DTA analyzer (Perkin-Elmer). The samples were heated from room temperature to 700 °C at a rate of 10 °C min<sup>-1</sup> in an air flow of 100 mL min<sup>-1</sup>.

Room temperature photoluminescence investigation was executed on the Fluorolog3 photoluminescence spectrometer (Horiba Jobin Yvon, Japan). The excitation wavelength is 325 nm, and the spectra were recorded in the range from 350 to 600 nm.

### 2.3. Evaluation of photocatalytic performance

For photocatalytic activity evaluation, the photodegradation of Rhodamine B was employed as a model reaction. Each time, the catalyst (20 mg) was suspended in aqueous solution of Rhodamine B ( $1.0 \times 10^{-5}$  mol L<sup>-1</sup>, 100 mL), and then the mixture was put into a beaker and agitated overnight in the dark to achieve the adsorption equilibrium on the catalyst surface. A 250 W high-pressure mercury lamp with a quartz condenser tube around was positioned in the middle of the beaker as UV irradiation source. Each degradation experiment was continuously conducted for 50 min, the mixture (3.5 mL) was withdrawn for analysis every 10 min. After separating the catalyst from the suspensions by centrifugation, the after-photoreacted solution was analyzed by a UV–vis spectrophotometer (Lambda 750S, Perkin-Elmer) with deionized water as reference (measuring the absorption of Rhodamine B at 554 nm). The catalyst degradation efficiency is calculated using the following equation:

$$\text{degradation (\%)} = \frac{(C_0 - C) \times 100}{C_0} = \frac{(A_0 - A) \times 100}{A_0}$$

$C_0$  and  $C$  are the initial and the changed concentrations of Rhodamine B, respectively; while  $A_0$  and  $A$  represent the initial and the changed absorbances of Rhodamine B at 554 nm, respectively [11].

## 3. Results and discussion

### 3.1. Characterization results

Fig. 1(a) shows the XRD patterns of as-synthesized sample ZnO-f and that doped with 5% Ag (ZA5), and Fig. 1(b) is the XRD patterns of all the as-synthesized pure ZnO samples with different morphologies. Only wurtzite-structured (hexagonal) ZnO (JCPDS 36-1451) is detected for the samples without Ag; while for the sample doped with 5% Ag, face-centered-cubic (FCC) metallic Ag (JCPDS 04-0783) is also identified except for hexagonal ZnO phase, but no obvious shift for the diffraction peaks of ZnO is observed, indicating that no solid solution between Ag and ZnO is formed [12]. In addition, the existence of metallic Ag in the sample ZA5 can also be confirmed by the UV–vis absorption spectra (Supplementary Data S1).

A low-magnification image of as-synthesized ZnO-f is shown in Fig. 2(a). It is clear that the sample is composed of lots of fluffy spheres with the diameter in the range of 2–3  $\mu\text{m}$ . To know more about this strange structure, the middle part of the sphere is magnified and presented in Fig. 2(b). It is found that the ZnO sphere is constructed by lots of crossed nanosheets with average thickness of  $\sim 20$  nm and a large amount of “hollow lattice” present inside the sphere. Apparently, the synthesized ZnO-f possesses a 3D hierarchical micro/nanostructure with a specific crossed arrangement of nanosheets.

After doped with Ag, as shown in Fig. 3(a), the sample still keeps the fluffy structure but with some nanoparticles scattering on the surface. The average diameter of these nanoparticles is about 20 nm. Fig. 3(b) shows the TEM image taken from the side of one nanosheet with nanoparticles attached on it. It is found that these particles are strongly attached on the surface of the nanosheet even after ultrasonic processing and electron beam attacking during TEM test. The EDX analysis on the interface, as seen in Fig. 3(c), confirms that these nanoparticles are only composed of Ag and Zn elements (Cu comes from copper grid), which is consistent with the XRD results. In a summary, Ag has been successfully doped into the fluffy ZnO-f via a facile one-pot synthesis method; the presence of Ag does not destroy such fluffy structure. In addition, the results of FT-IR spectra and TG further indicate that there are no organic compounds residual in ZnO-f and ZA5 (Supplementary Data S2, S3).

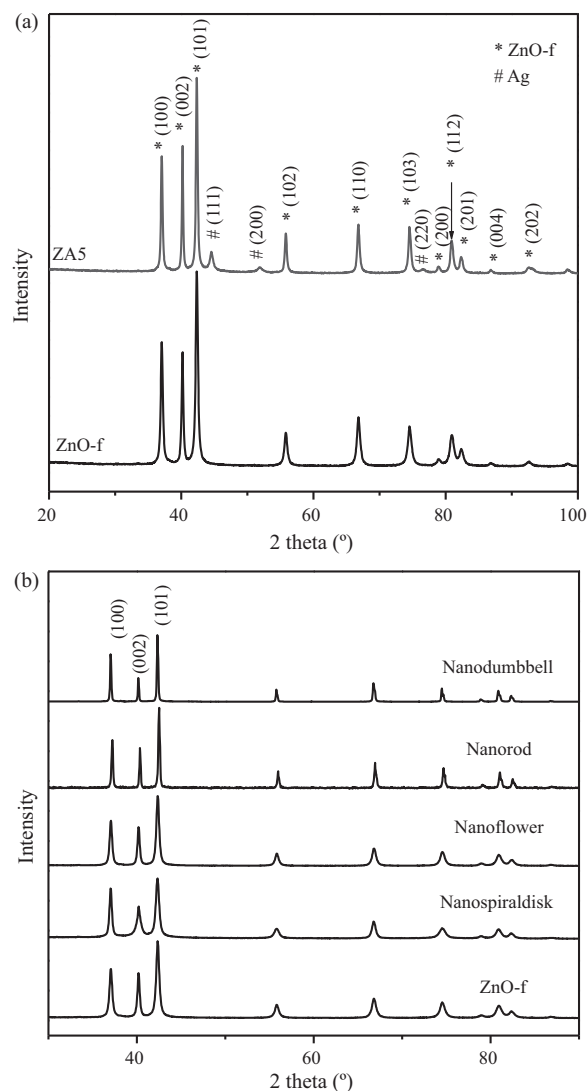
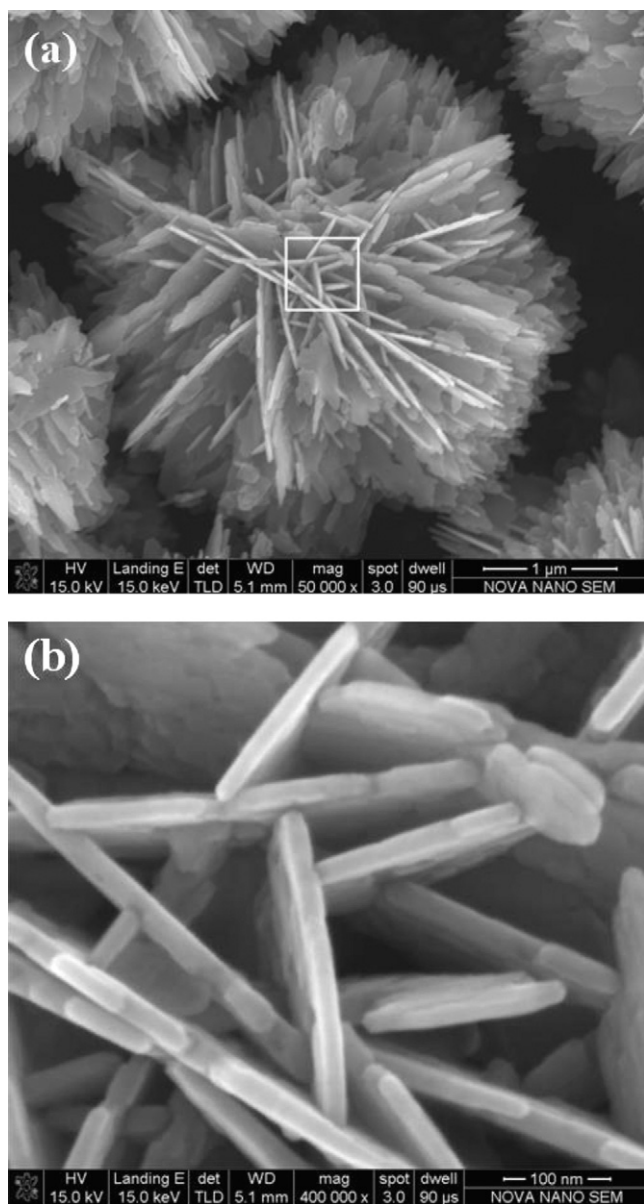


Fig. 1. (a) XRD patterns of the as-synthesized ZnO sample (ZnO-f) and that doped with 5% Ag (ZA5). (b) The XRD patterns of all the as-synthesized pure ZnO samples.

The specific surface area and pore size distribution of the samples are measured by nitrogen adsorption/desorption. Full nitrogen sorption isotherms of the fluffy ZnO-f and the sample ZA5 are shown in Fig. 4(a). They are all similar to the type II isotherm with the hysteresis loops: when the relative pressure ( $P/P_0$ ) reaches 0.4, the adsorption volume upticks and the desorption hysteresis occurs because of the capillary condensation of nitrogen in pores [13]. Fig. 4(b) shows pore diameter distribution determined by Barrett–Joyner–Halenda (BJH) method from the desorption branch of the isotherm. It can be seen that most of the pores possess diameters in the range of 2–30 nm with the peak zenith appearing around 12 nm. The specific surface area ( $S_{\text{BET}}$ ) calculated by BET method is  $42 \text{ m}^2 \text{ g}^{-1}$  for ZnO-f and  $37 \text{ m}^2 \text{ g}^{-1}$  for ZA5, much larger than those for the samples synthesized via wet chemical methods [2,14].

Fig. 5 shows the XPS spectra of as-synthesized samples. There are no peaks for other elements except Zn, O, Ag and C observed from the full XPS spectra as shown in Fig. 5(a). Compared with that of pure metallic Ag, the binding energy of Ag  $3d_{5/2}$  for ZA5 shows a prominent shift from 367.93 to 367.49 eV, implying a strong interaction between Ag and ZnO. The binding energy shift and the interaction mechanism may be explained by band theory as shown in Scheme 1(a). The Fermi energy level of Ag is higher than that of



**Fig. 2.** (a) A low-magnification image of the fluffy ZnO sphere (ZnO-f) and (b) a high-magnification image of the middle part of the fluffy ZnO sphere marked in (a).

ZnO. When Ag and ZnO interact, new Fermi energy level is formed to keep stable state. The free electrons above the new Fermi energy level of Ag could flow into ZnO causing the electron deficiency of Ag [3,12,15,16], partially generating monovalent Ag in ZA5, which possesses a lower binding energy of Ag  $3d_{5/2}$  as compared with  $Ag^0$ .

For O1s, two peaks ( $\alpha$  and  $\beta$ ) are identified, indicating two different kinds of O species, as shown in Fig. 5(c). The peak  $\alpha$  should be associated with the lattice oxygen of ZnO ( $O_l$ ) while the peak  $\beta$  may be arising from the chemisorbed oxygen ( $O_a$ ) caused by surface hydroxyl groups [12]. The existence of surface hydroxyl groups can be further confirmed by FT-IR spectra as shown in Supplementary Data S2. The XPS analysis results for the fluffy ZnO-f and all the samples doped with Ag are listed in Table 1. The surface atomic ratio between O and Zn (O/Zn) is calculated from the full XPS spectra. The O/Zn ratio increases from 0.69 to 3.27 with the content of Ag increasing, suggesting a transformation from oxygen deficiency to excess oxygen in these samples (the full XPS spectra for ZnO and all the ZA samples together with the explanation of this change are

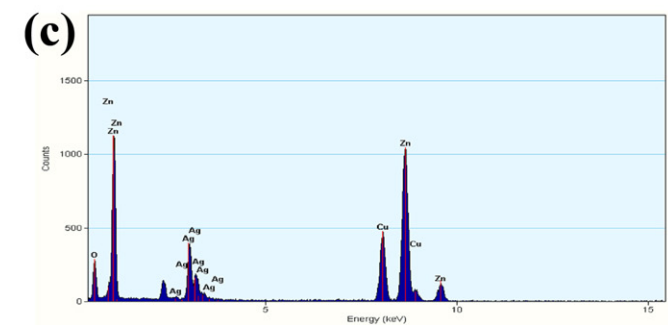
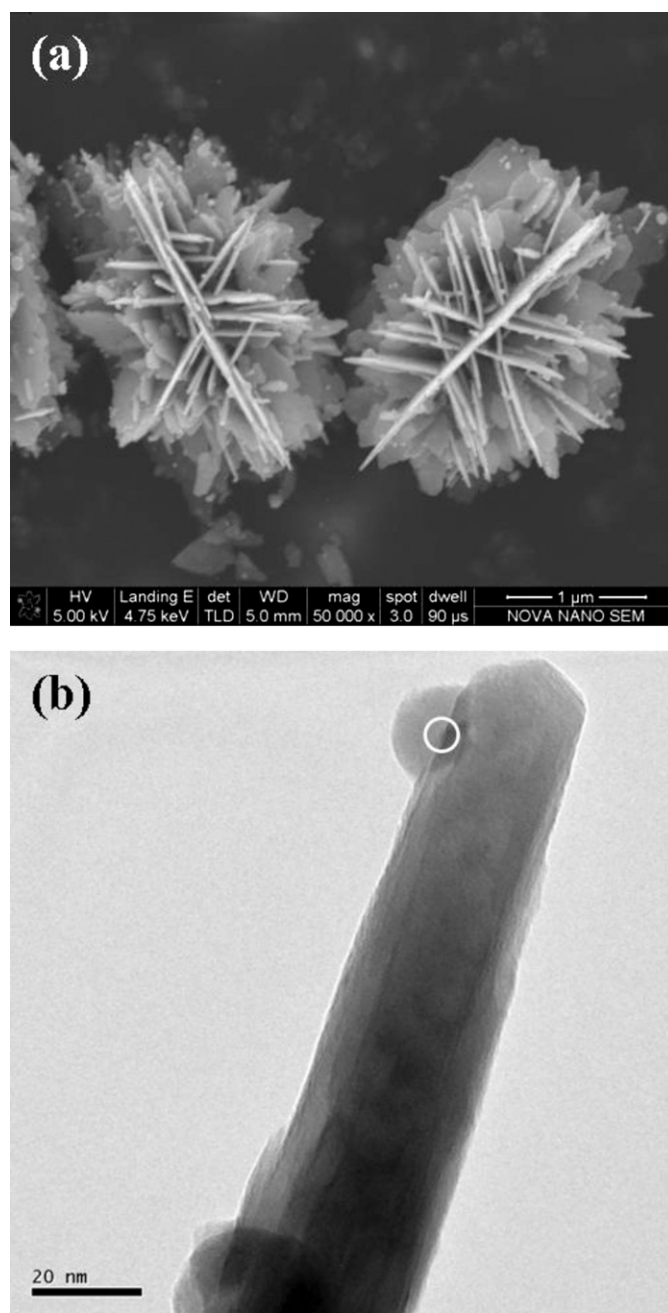


**Fig. 3.** (a) The SEM image of the sample doped with 5% Ag (ZA5); (b) the TEM image taken from the side of one nanosheet with nanoparticles attached on it; (c) EDX analysis of the area marked with white circle in (b).



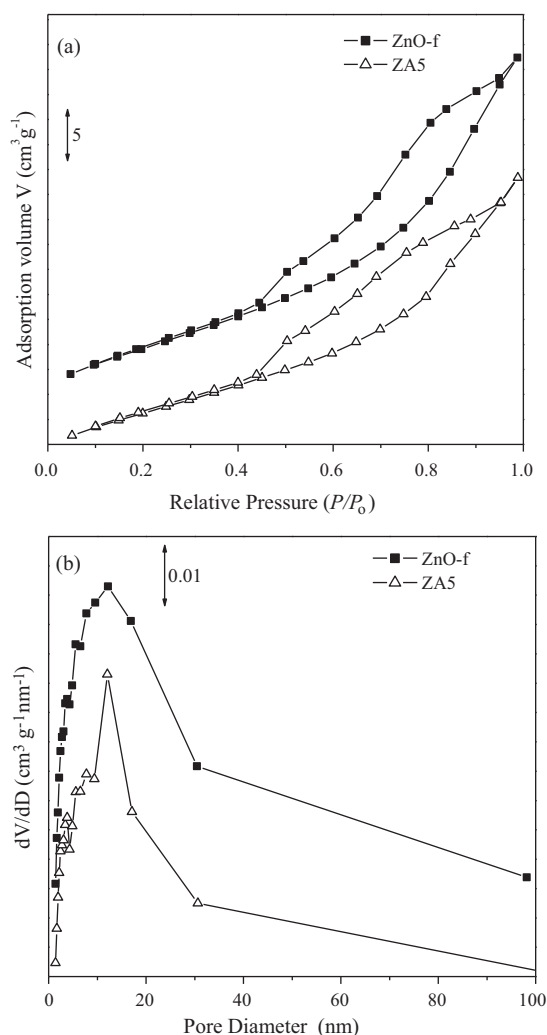


**Fig. 4.** (a)  $N_2$  adsorption/desorption isotherms of ZnO-f and ZA5 and (b) BJH pore diameter distribution of ZnO-f and ZA5.

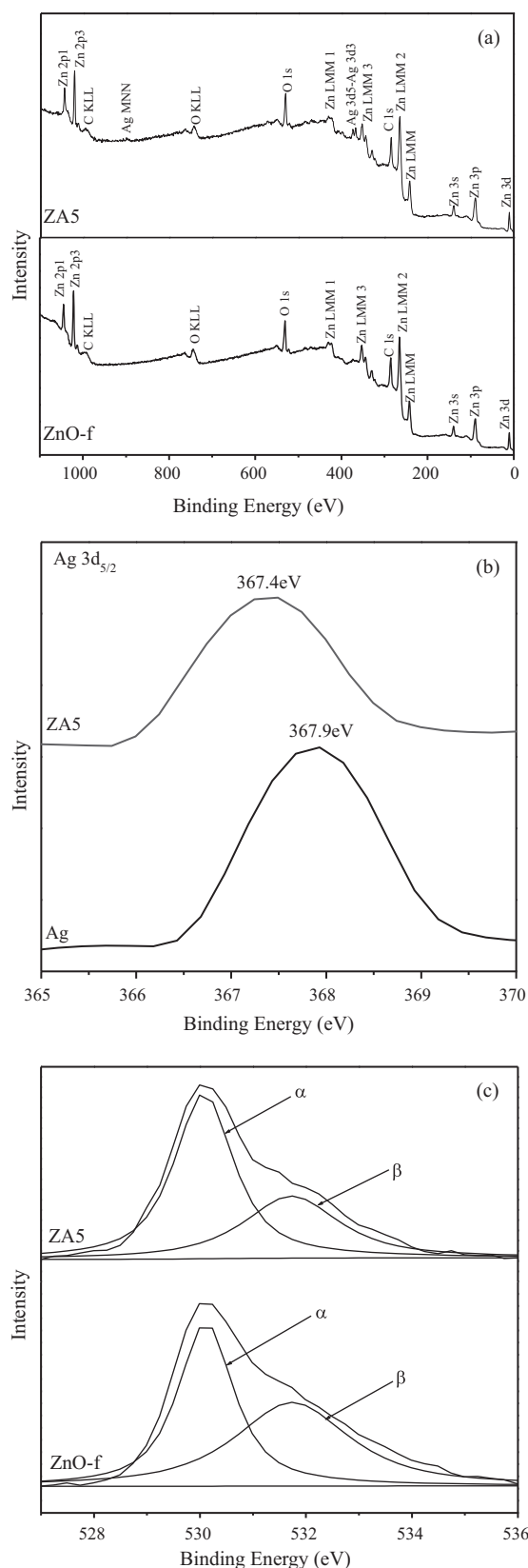
available in [Supplementary Data S4](#)). It is clear that the doping of Ag can easily modify the surface O species of ZnO-f.

Fig. 6(a) is the room temperature photoluminescence spectra of the pure ZnO catalysts with different morphologies. The excitation wavelength is 325 nm, and the spectra were recorded in the range from 350 to 600 nm. Fig. 6(b) is the amplified spectra of Fig. 6(a) in the region of 350–390 nm. The strong ultraviolet emission around 367 nm as shown in Fig. 6(b) is due to the near band edge emission of ZnO (3.37 eV) which is corresponding to the electron–hole recombination between valence band and conduction band [1]. The stronger the ultraviolet emission is, the easier the electron–hole recombination is, and the lower the electron–hole segregation efficiency is. The visible light emission is usually attributed to different

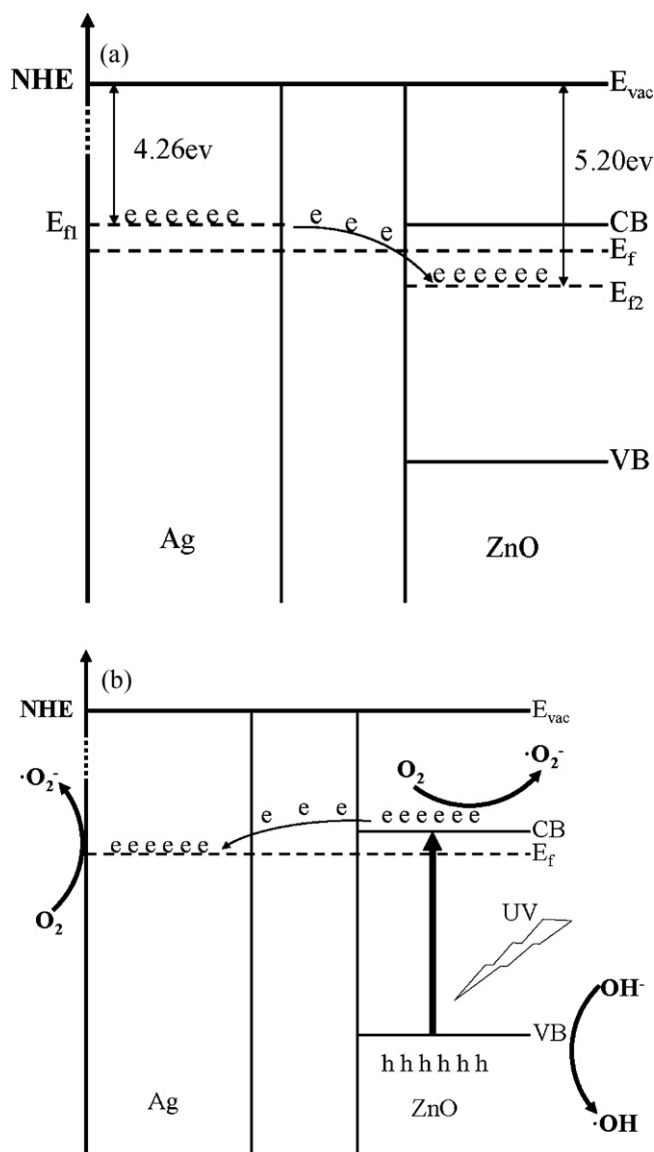
**Table 1**

XPS analysis results: Ag%, Zn% and O% are the atomic percentage of surface Ag, Zn and O, respectively calculated from full XPS spectra.  $O_i/O_a$  (lattice oxygen/chemisorbed oxygen) is calculated from the peak area ratio of  $\alpha/\beta$ .

Samples	Ag%	Zn%	O%	O/Zn	$O_a/O_i$	$O_a\%$
ZnO-f	0	59.1	40.9	0.69	0.81	18.3
ZA1	1.2	54.9	43.9	0.80	1.25	24.4
ZA3	2.1	50.2	47.7	0.95	1.51	28.7
ZA5	2.9	35.1	62.0	1.77	1.74	39.4
ZA7	4.3	30.1	65.6	2.18	0.61	24.8
ZA9	5.6	22.1	72.3	3.27	0.49	23.8



**Fig. 5.** XPS spectra of as-synthesized ZnO-f and ZA5: (a) full XPS spectra; (b) Ag  $3d_{5/2}$  spectra; (c) O 1s spectra.

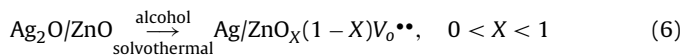
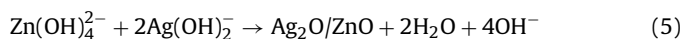
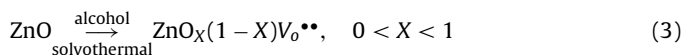


**Scheme 1.** (a) Electrons transfer from Fermi energy level of Ag ( $E_{f1}$ ) to that of ZnO ( $E_{f2}$ ) to get equilibrium and form new Fermi energy ( $E_f$ ) and (b) the formation of electron-hole pairs and the photocatalytic degradation mechanism under UV light irradiation (NHE: normal hydrogen electrode;  $E_{vac}$ : vacuum energy level;  $e^-$ : electron,  $h^+$ : hole.).

defects of the material. Comparing with other pure ZnO samples, the emission spectra of the ZnO-f is very smooth in the visible light region, indicating the well crystallinity of the fluffy ZnO spheres [10].

### 3.2. Growth mechanism

Generally, the chemical reactions in the solvothermal system for the formation of ZnO or Ag/ZnO can be formulated as follows [14,17]:



Eqs. (4)–(6) are only for the case with the addition of Ag. The chemical equilibrium of Eq. (2) is a key step for the formation of ZnO precursor. In this work the molar ratio of  $OH^-/Zn^{2+}$  was more than 4:1 and the concentration of  $OH^-$  is very high. In such alkali solution, the ZnO precursor is very difficult to form at ambient condition because the chemical equilibrium of Eq. (2) shifts to the left easily. Therefore, during solvothermal synthesis, alcoholic solvent is used to deactivate the  $OH^-$  and control the equilibrium of Eq. (2), making it shift to the right. Low-concentration  $Zn^{2+}$  and high-concentration  $OH^-$  react in this alcoholic solvent can easily slow the growth of ZnO which is very important for the formation of such fluffy structure. It is well known that ethanol is a weak reducing agent under high temperature and pressure. When the ZnO precursor is exposed to the solvothermal surrounding (alcoholic solvent, at 120 °C for 24 h), the surface oxygen of ZnO can be deprived by ethanol, leading to the generation of surface oxygen vacancy ( $V_o^{\bullet\bullet}$ ) on ZnO nanocrystals (Eq. (3) or Eq. (6)).

Normally, ZnO crystallites with the hexagonal wurtzite structure (belong to the space group of  $P6_3mc$ ) are polar because the

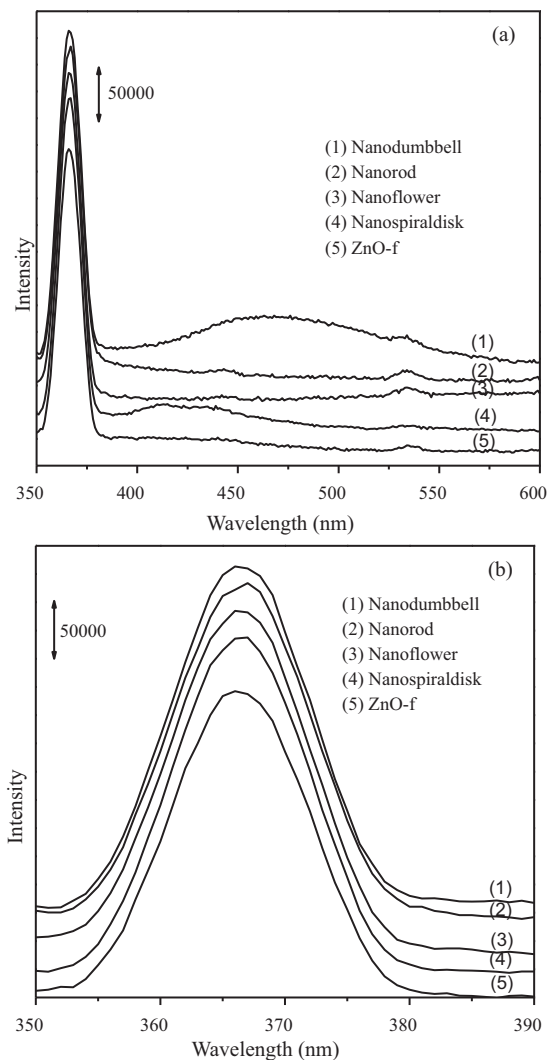
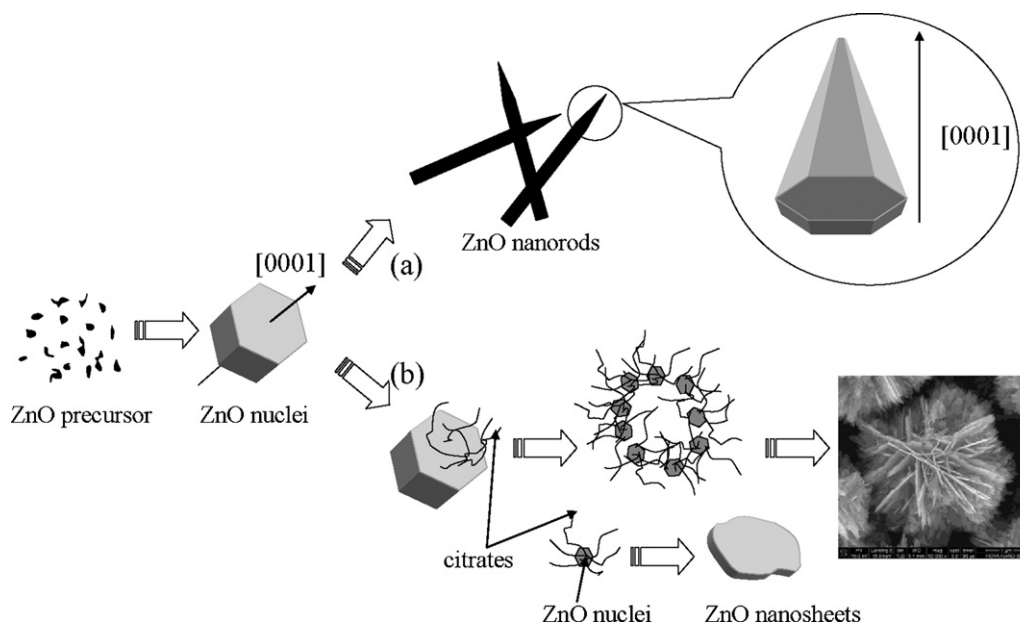


**Fig. 6.** Room temperature photoluminescence emission spectra of the pure ZnO samples with different morphologies: (a) full spectra from 350 to 600 nm; (b) ultra-violet emission spectra from 350 to 390 nm.



**Scheme 2.** (a) ZnO grows along the [0001] crystal axis and (b) a potential mechanism for the formation of the fluffy ZnO sphere.

Zn ions and O ions combine together via tetrahedral coordination, causing the polar symmetry along the hexagonal axis. It is well known that there are two polar planes for ZnO crystallites: one is the positive polar plane terminated by Zn (0001) and another is the negative polar plane terminated by O (000 $\bar{1}$ ) [18]. In general, the Zn-terminated ZnO plane is very active due to its high surface energy [19]. As a result, the ZnO crystallites grow very fast along [0001] direction (*c*-axis), enhancing the formation of nanowires or nanorods, as described in Scheme 2(a). For comparison, the nanorod was also synthesized in the same system without addition of citric acid. Fig. 7(a) shows one of the well-defined ZnO nanorods which are hexagonal prisms with seamed edge clearly distinguished. The high-magnification image in Fig. 7(b) shows that the interplanar spacing of the nanorod is 0.26 nm corresponding to the *d*-spacing of (002) plane of ZnO, which indicates that the nanorod grows along the [0001] direction (*c*-axis). The growth mechanism for these nanorods is illuminated in Scheme 2(a).

If citric acid is added to the solvothermal system, the situation is different. Scheme 2(b) describes the formation process of this fluffy structure. On the one hand, the citric acid and the zinc ion can readily form chelate ring complex because of the existence of carboxyls and hydroxyls in citric acid [20]; on the other hand, ethanol can reduce the ZnO precursor, promoting the generation of surface oxygen vacancy under solvothermal condition as discussed above. In such a case, the interaction between  $\text{Zn}^{2+}$  and citric acid is enhanced because more  $\text{Zn}^{2+}$  terminal surfaces are exposed during the growth process. This interaction greatly decreases the surface energy of the Zn-terminated plane, suppressing the growth along [0001] direction. As a result, the ZnO precursors grow along other directions, forming ZnO nanosheets other than nanowires or nanorods. In addition, since the growth speeds of different side surfaces are various the edges of these nanosheets are irregular. Moreover, it is reported that the ZnO nuclei bound by citric acid can form colloidal clusters [21,22], in which each ZnO nucleus grows to irregular nanosheets with the citric acid still attaching on its surface. The attachment of citric acid as the capping agent is very significant for the stability of the colloidal clusters. In this solvothermal system, the citric acid not only prevents the mergence between these small colloidal clusters, but also provides steric hindrance in the colloidal clusters. This can well account for that why there are lots of hollow lattices in the fluffy ZnO-f sphere. Fig. 7(c) is the low-

magnification TEM image of a fragment from a fluffy ZnO-f sphere. It is clearly seen that these nanosheets strew at random and cross together which is consistent with the SEM image in Fig. 2. The high-magnification TEM image for the side of one nanosheet is shown in Fig. 7(d). The distinguished interplanar spacing is 0.26 nm which is the *d*-spacing of (002) plane of ZnO. This is to say, the [0001] direction (*c*-axis) is the normal direction of the nanosheets, which confirms that the growth along [0001] direction in the solvothermal system is suppressed after citric acid is added.

Fig. 7(e) shows the image of the sample synthesized without ethanol but with other synthesis conditions unchanged. It can be seen that this sample is composed of many irregular spheres. Although the [0001] direction is suppressed, there are no crossed nanosheets, since in this condition the functions of citric acid are weakened, and the colloidal clusters can more easily aggregate during growth.

Fig. 7(f) presents the image of the sample synthesized in the absence of both ethanol and citric acid but with other synthesis conditions unchanged. It can be seen that this sample is composed of many flowerlike blocks which assemble together irregularly, no fluffy structure can be found. The absence of ethanol, which is regarded as an important weak reducing agent in the solvothermal system, significantly decreases the surface oxygen vacancy ( $\text{V}_{\text{O}}^{\bullet\bullet}$ ) of ZnO, thus influencing the adsorption of citric acid on its surface. As a result, the two functions of citric acid mentioned above have disappeared, making the fluffy structure hardly fabricated in this condition.

In a summary, the synergistic effect of ethanol and citric acid on ZnO in the solvothermal system is crucial to the formation of such specific fluffy structure.

### 3.3. Photocatalytic performance

Fig. 8 shows the photocatalytic activity of pure ZnO and Ag/ZnO catalysts. For comparison, the blank test was also conducted under the same reaction condition. It can be seen that the degradation rate of Rhodamine B is very low in the absence of catalysts under UV irradiation for 50 min. With the addition of catalysts, the degradation is greatly accelerated.

Fig. 8(a) shows the influence of ZnO morphology on the photocatalytic activity for Rhodamine B degradation. It can be

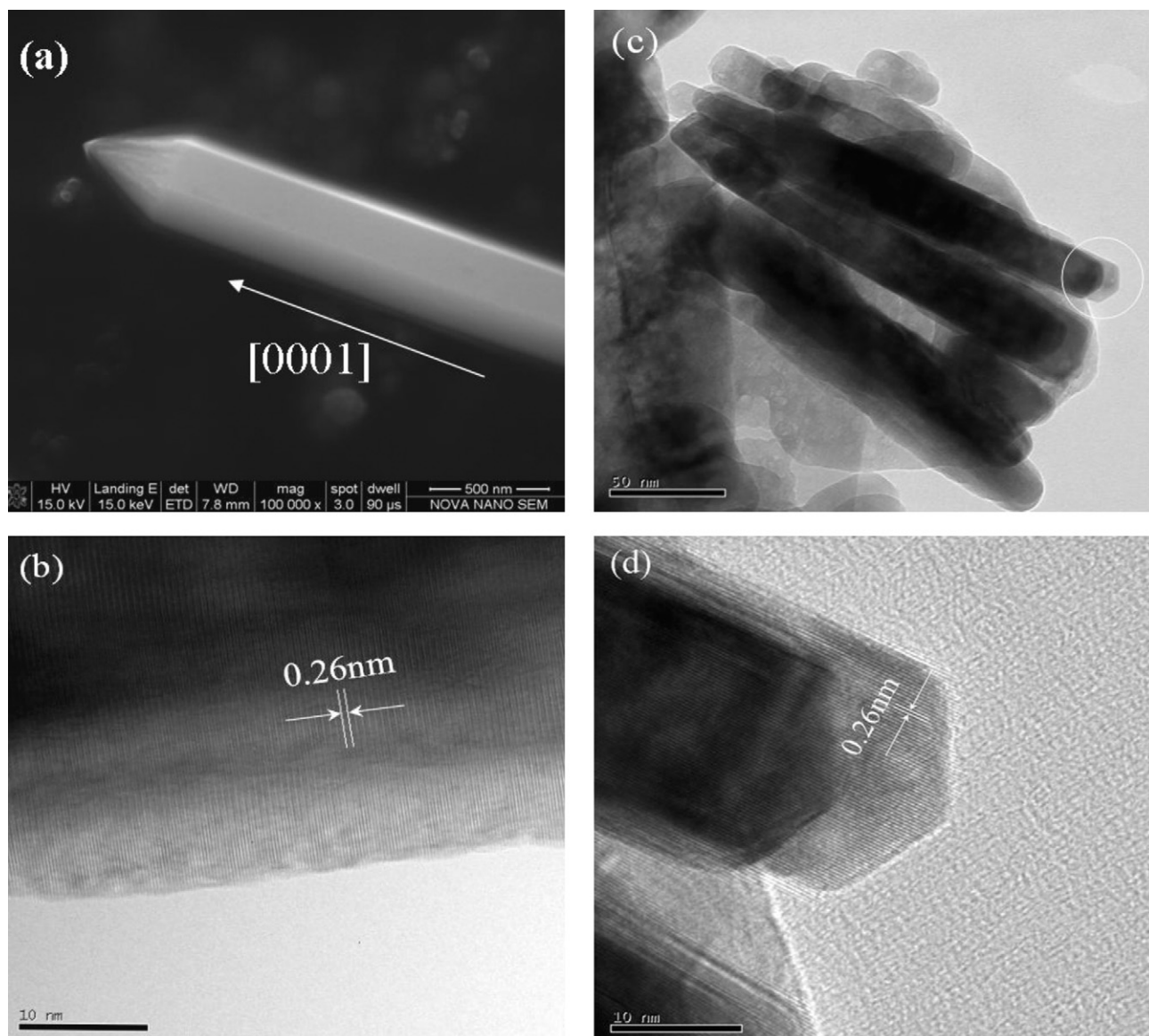


**Fig. 7.** The influence of ethanol and citric acid on the morphology of ZnO: (a) SEM image of the nanorod synthesized without using citric acid; (b) HR-TEM image of the nanorod synthesized without using citric acid; (c) low-magnification TEM image for a fragment of one broken ZnO sphere with fluffy structure; (d) a high-magnification image of the region marked with white circle in (c); (e) SEM of the sample synthesized without using ethanol; (f) SEM of the sample synthesized without using ethanol and citric acid.

seen that the fluffy ZnO-f shows much better photocatalytic activity than other as-synthesized nanostructured ZnO catalysts whose SEM images are shown in [Supplementary Data S5](#). The linear fitting plots of  $-\ln(C_t/C_0) = f(t)$  for pure ZnO catalysts with different morphologies are shown in [Fig. 8\(b\)](#), where  $C_0$  and  $C_t$  are the initial concentration of Rhodamine B after the equilibrium adsorption and the reaction concentration of Rhodamine B at time  $t$ , respectively. It is found that the squares of linear correlation coefficients ( $R^2$ ) are all more than 98%, so the photodegradation of Rhodamine B can be considered as a pseudo-first-order reaction in kinetics and the slope of the linear  $-\ln(C_t/C_0) = f(t)$  can be considered as the rate constant  $k$ . For comparison, the rate constants for the blank reaction and all the pure ZnO catalysts are listed in [Table 2](#). From the rate constant  $k$  in [Table 2](#), it can be deduced that the order for the photodegradation rates ( $r$ ) over the pure ZnO with different morphologies is:  $r(\text{ZnO-f}) > r(\text{nanoflower}) > r(\text{nanospiraldisk}) > r(\text{nanorod}) > r(\text{nanodumbbell})$ .

The ultraviolet emission peak areas calculated from the room temperature photoluminescence spectra ([Fig. 6](#)) for the

pure ZnO catalysts are also listed in [Table 2](#). It is found that the ultraviolet emission peak area increases in the order of  $\text{ZnO-f} < \text{nanospiraldisk} < \text{nanoflower} < \text{nanorod} < \text{nanodumbbell}$ . It is well known that the strong ultraviolet emission corresponds to the high electron-hole recombination. That is to say, the ZnO-f with fluffy structure shows much higher electron-hole segregation efficiency than other as-synthesized nanostructured ZnO catalysts, which is an important reason for its much better photocatalytic activity.

Besides the segregation efficiency of electrons and holes, the surface area of the ZnO-f is also an important factor for its better photodegradation activity. The ZnO-f with hollow fluffy structure possesses the largest specific surface area, thus providing the largest number of active sites during the photocatalytic reaction; meanwhile, such hollow fluffy structure is favorable to mass transport and adsorption of Rhodamine B which occurs not only on the outside surface of the catalyst but also on the wall of the inside lattices. On the contrary, low surface area means less available active sites, limiting the adsorption activation of



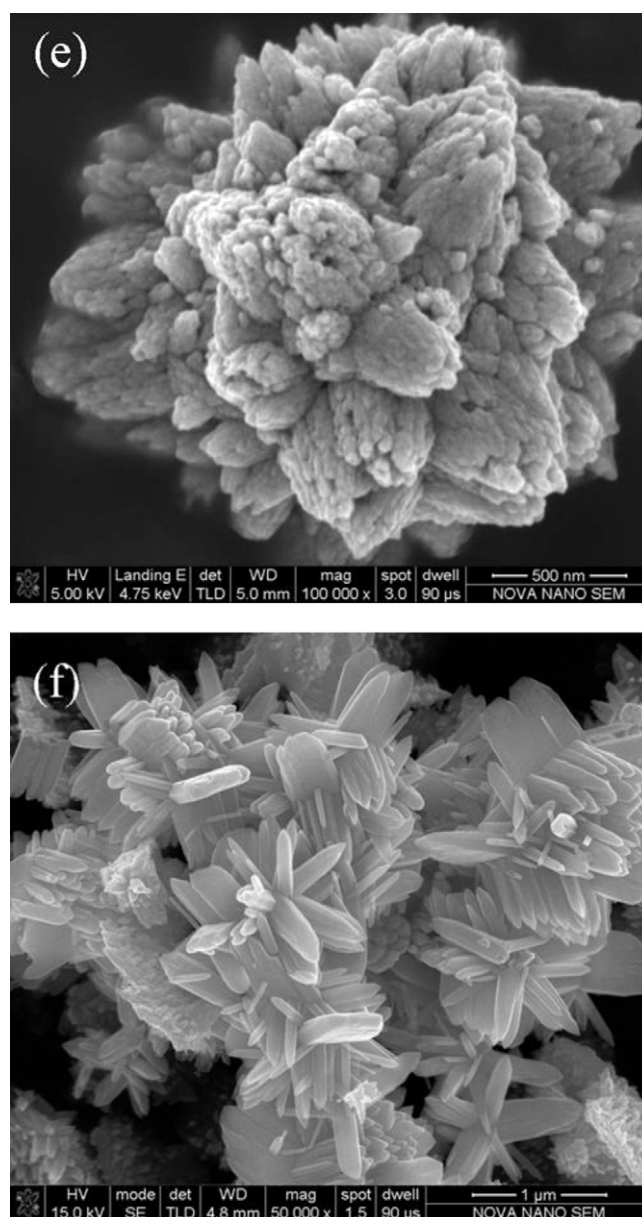


Fig. 7. (Continued)

reactants on the catalyst. The effect of surface area for ZnO-f on the photocatalytic activity can be confirmed by the order of normalized photodegradation rates (Supplementary Data S6). As seen in Table 2, the increasing order of the ultraviolet emission peak area is nearly the same with the decreasing order of photodegradation rate except nanospiraldisk. Although the electron–hole segregation efficiency of the nanospiraldisk is higher than that of nanoflower, the photodegradation activity of nanospiraldisk is

lower than that of nanoflower, probably due to its much lower surface area. In addition, Table 2 shows the crystallinity of these nano-materials. It can be found that the order of the crystallinity (ZnO-f > nanoflower > nanorod > nanodumbbell > nanospiraldisk) is nearly the same as that of  $k$  except nanospiraldisk. The crystallinity of nanospiraldisk is the lowest. Perhaps, there are some inactive amorphous phases in the nanospiraldisk which also decrease its photodegradation activity.

**Table 2**

The specific surface area ( $S_{\text{BET}}$ ), ultraviolet emission peak area, reaction rate constant ( $k$ ) for Rhodamine B photodegradation and the crystallinity of pure ZnO with different morphologies ( $R^2$  represents the square of correlation coefficient of kinetics linear fitting).

Sample	$S_{\text{BET}}$ ( $\text{m}^2 \text{g}^{-1}$ )	Ultraviolet emission peak area	$k$ ( $\text{min}^{-1}$ )	Crystallinity <sup>a</sup> (%)	$R^2$
Blank			0.0029		0.9990
Nanodumbbell	13	4,668,697	0.0174	94.85	0.9984
Nanorod	14	4,618,153	0.0180	95.52	0.9992
Nanoflower	17	4,598,289	0.0225	99.26	0.9831
Nanospiraldisk	5	4,520,528	0.0186	88.80	0.9965
ZnO-f	42	4,192,839	0.0332	99.29	0.9926

<sup>a</sup> The crystallinity of each sample is calculated from their XRD data by dividing the total peak area of ZnO crystal phase with the total area of all the diffraction peaks.

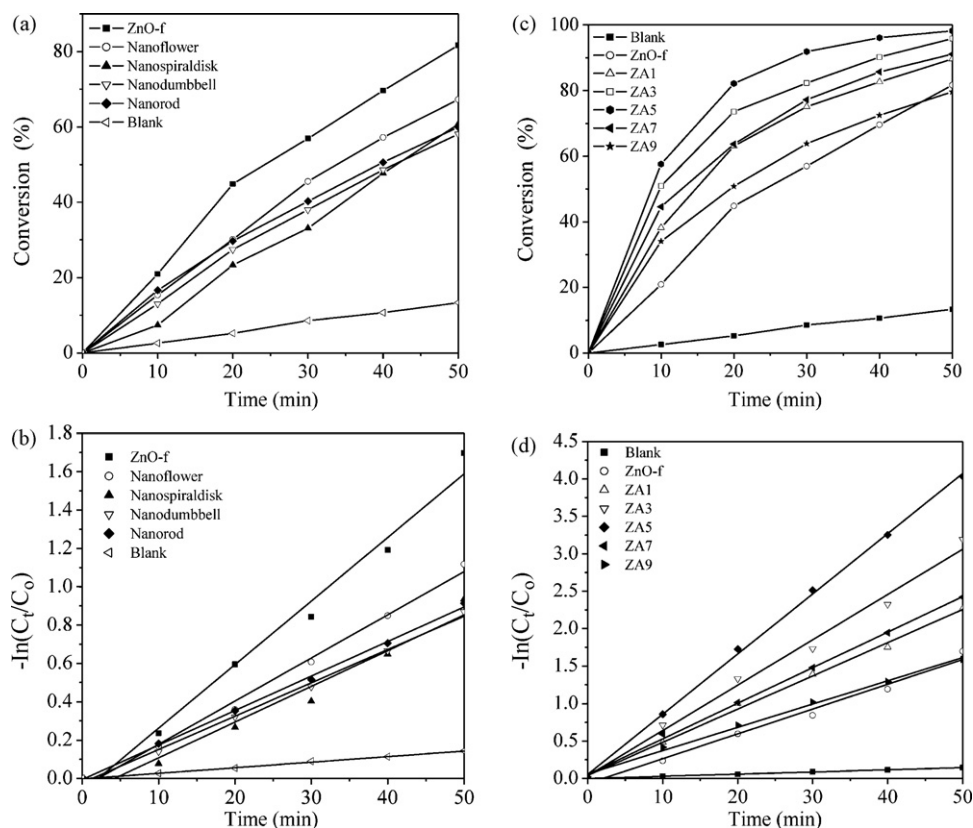


**Fig. 8.** Photocatalytic activity and kinetics of the samples for Rhodamine B degradation. (a) and (b) Pure ZnO with different morphologies; (c) and (d) Ag/ZnO with different contents of Ag.

After doped with Ag, the photocatalytic activity of ZnO is prominently enhanced, as shown in Fig. 8(c). It has been reported that the coupled noble metal-semiconductor photocatalysts often exhibit high electron-hole segregation efficiency because the noble metals can serve as a sink for electrons, thus enhancing the photocatalytic activity of the catalysts. The electron migration process and the photocatalytic mechanism over Ag/ZnO catalyst can be briefly described by Scheme 1(b). After irradiated by UV light with the energy equal to or higher than the band gap of ZnO, the electrons in the valence band (VB) of ZnO can be excited into the conduction band (CB), leading to the separation of electrons and holes. Since the Fermi energy level of Ag is lower than the energy level for the conduction band (CB) of ZnO, the excited electrons can flow into the Fermi energy level of Ag, which effectively promotes the separation of electrons and holes. Over Ag sites these excited electrons can be further captured by  $O_2$  to form superoxide radical anion  $\cdot O_2^-$ , while the holes can be captured by  $OH^-$  to form hydroxide free radical  $\cdot OH$ , which are crucial to the degradation of organic dyes [3,12,14].

Fig. 8(d) shows the linear plots of  $-\ln(C_t/C_0) = f(t)$  for ZA catalysts, and Table 3 lists the rate constants. From the rate constants in Table 3, it can be inferred that the order for the photodegradation rates ( $r$ ) over the catalysts with different Ag contents is:  $r(ZA5) > r(ZA3) > r(ZA7) > r(ZA1) > r(ZnO-f) > r(ZA9)$ . It is obvious that the presence of Ag really accelerates the photodegradation reaction and the optimized content of Ag is 5%, however, too much Ag results in a decrease of the photocatalytic activity, such as ZA9, which is even less active than ZnO-f. Although Ag doping can effectively enhance the segregation efficiency of electrons and holes, the photocatalytic activity is also influenced by other factors. Firstly, too much Ag can occupy most of the surface of ZnO and reduce the availability of UV light, thus lowering the photocatalytic activity; secondly, the overloading of Ag can block the hollow lattices and decrease the specific surface area of the catalyst. From Table 3 it can

be seen that the specific surface area of the catalysts remarkably decreases as the content of Ag is higher than 5%.

Combined with the XPS results, it is found that the catalytic performance of the catalysts is not only related to their specific surface area, but more dependent on the amounts of surface chemisorbed oxygen species. The photocatalytic activity of these catalysts is well correlated with the amounts of chemisorbed oxygen ( $O_a\%$ ) when the content of Ag is lower than 9%, that is to say, the larger amount of chemisorbed oxygen, the higher photocatalytic activity (as listed in Table 3). The importance of the surface chemisorbed oxygen is illustrated in Scheme 1(b): they can capture holes to form  $\cdot OH$  radicals and promote the adsorption of  $O_2$  to form  $\cdot O_2^-$  which play a significant role in degrading the organic dyes [3,12,14]. But for ZA9, too much Ag covers the surface of ZnO which reduces the specific surface area and the availability of UV light, as a result, the yields of electrons and holes during UV irradiation are very low. Although the amount of chemisorbed oxygen over ZA9 is larger than that over ZnO-f, it possesses lower photocatalytic activity, just due to the smaller amount of holes in ZA9.

**Table 3**

The specific surface area ( $S_{BET}$ ), the atomic percentage of surface chemisorbed oxygen ( $O_a\%$ ) and reaction rate constant ( $k$ ) for Rhodamine B photodegradation over Ag/ZnO with different contents of Ag ( $R^2$  represents the square of correlation coefficient of kinetics linear fitting).

Sample	$S_{BET}$ ( $m^2 g^{-1}$ )	$O_a\%$	$k$ ( $min^{-1}$ )	$R^2$
Blank			0.0029	0.9990
ZnO-f	42	18.3	0.0332	0.9926
ZA1	38	24.4	0.0444	0.9985
ZA3	37	28.7	0.0606	0.9952
ZA5	37	39.4	0.0804	0.9999
ZA7	28	24.8	0.0475	0.9991
ZA9	17	23.8	0.0311	0.9977

#### 4. Conclusions

Nanosheets-constructed ZnO spheres with novel three-dimensional (3D) fluffy structure can be successfully synthesized by a facile one-step solvothermal method. The synergistic effect of ethanol and citric acid is crucial to the formation of such fluffy ZnO. This easy and economy method can be potentially popularized for the synthesis of other composite materials with hollow structure inside.

The higher electron–hole segregation efficiency and the novel 3D structure with larger specific surface area make the fluffy ZnO spheres possess much better photocatalytic performance for the degradation of Rhodamine B as compared with other commonly reported nanostructured ZnO materials, such as nanoflowers, nanospiraldisks, nanodumbbells and nanorods.

Ag can be readily doped on the surface of the ZnO spheres without destroying the fluffy structure. The interaction between Ag and ZnO remarkably enhances the photocatalytic activity of ZnO. The catalytic performance of the Ag/ZnO catalysts is not only determined by their specific surface area, but more dependent on the amounts of surface chemisorbed oxygen species. The catalyst doped with 5% Ag possesses the largest amount of surface chemisorbed oxygen, showing the highest photocatalytic activity for the degradation of Rhodamine B.

#### Acknowledgements

This work is financially supported by the National Natural Science Foundation of China (No. 20876110 and 21076146), the Specialized Research Fund for the Doctoral Program of Higher Education of China (No. 20090032110013) and the Program of New Century Excellent Talents in University of China (No. NCET-07-0599). The authors are also grateful to the Cheung Kong Scholar Program for Innovative Teams of the Ministry of Education (No.

IRT0641) and the Program of Introducing Talents of Discipline to University of China (No. B06006).

#### Appendix A. Supplementary data

Supplementary data associated with this article can be found, in the online version, at doi:10.1016/j.apcatb.2010.08.027.

#### References

- [1] D.M. Bagnall, Y.F. Chen, Z. Zhu, T. Yao, *Appl. Phys. Lett.* 73 (1998) 1038–1040.
- [2] M.J. Height, S.E. Pratsinis, O. Mekasuwandumrong, P. Praserttham, *Appl. Catal. B* 63 (2006) 305–312.
- [3] W.W. Lu, S.Y. Gao, J.J. Wang, *J. Phys. Chem. C* 112 (2008) 16792–16800.
- [4] C.J. Murphy, N.R. Jana, *Adv. Mater.* 14 (2002) 80–82.
- [5] Q. Wan, T.H. Wang, *Appl. Phys. Lett.* 87 (2005) 83105.
- [6] F. Lu, W.P. Cai, Y.G. Zhang, *Adv. Funct. Mater.* 18 (2008) 1047–1056.
- [7] B. Liu, H.C. Zeng, *J. Am. Chem. Soc.* 126 (2004) 16744–16746.
- [8] Z.R. Tian, J.A. Voigt, J. Liu, B. McKenzie, M.J. Mcdermott, *J. Am. Chem. Soc.* 124 (2002) 12954–12955.
- [9] J. Yahiro, T. Kawano, H. Imai, *J. Colloid Interface Sci.* 310 (2007) 302–311.
- [10] R. Georgekutty, M.K. Seery, S.C. Pillai, *J. Phys. Chem. C* 112 (2008) 13563–13570.
- [11] Y.Y. Zhang, J. Mu, *J. Colloid Interface Sci.* 309 (2007) 478–484.
- [12] Y.H. Zheng, L.R. Zheng, Y.Y. Zhan, X.Y. Lin, Q. Zheng, K.M. Wei, *Inorg. Chem.* 46 (2007) 6980–6983.
- [13] K.S.W. Sing, *Pure & Appl. Chem.*, Pergamon Press Ltd., Great Britain, 1982, p. 2210.
- [14] Y.H. Zheng, C.Q. Chen, Y.Y. Zhan, X.Y. Lin, Q. Zheng, K.M. Wei, J.F. Zhu, *J. Phys. Chem. C* 112 (2008) 10773–10777.
- [15] G.Y. Shan, L.H. Xu, G.R. Wang, Y.C. Liu, *J. Phys. Chem. C* 111 (2007) 3290–3293.
- [16] M.K. Lee, T.G. Kim, W. Kim, Y.M. Sung, *J. Phys. Chem. C* 112 (2008) 10079–10082.
- [17] Y.H. Zheng, C.Q. Chen, Y.Y. Zhan, X.Y. Lin, Q. Zheng, K.M. Wei, J.F. Zhu, Y.J. Zhu, *Inorg. Chem.* 46 (2007) 6675–6682.
- [18] M. Ethayaraja, R. Bandyopadhyaya, *Langmuir* 23 (2007) 6418–6423.
- [19] Z.P. Fu, Z. Wang, B.F. Yang, Y.L. Yang, H.W. Yan, L.S. Xia, *Mater. Lett.* 61 (2007) 4832–4835.
- [20] Z. Yang, Q.H. Liu, H.C. Yu, B.S. Zou, Y.G. Wang, T.H. Wang, *Nanotechnology* 19 (2008) 35704.
- [21] S.Y. Gao, H.J. Zhang, X.M. Wang, R.P. Deng, D.H. Sun, G.L. Zheng, *J. Phys. Chem. B* 110 (2006) 15847–15852.
- [22] H. Zhang, D.R. Yang, Y.J. Ji, X.Y. Ma, J. Xu, D.L. Que, *J. Phys. Chem. B* 108 (2004) 3955–3958.